ELSEVIER

NDT&E International, Vol. 30, No. 4, pp. 205–210, 1997

Printed in Great Britain.
PII:S0963-8695(96)00057-6
0963-8695/97 $17.00+0.00

Electromagnetic and elastic wave scattering and inverse scattering applied to concrete

K. J. Langenberg, R. Bärmann, R. Marklein, S. Irmer, H. Müller, M. Brandfaß and B. Potzkai

Department of Electrical Engineering, University of Kassel, 34109 Kassel, Germany

Electromagnetic and elastodynamic scattering and inverse scattering techniques are combined to provide a better understanding of wave propagation and obstacle imaging in concrete. In particular we propose an electromagnetic inversion algorithm for ground probing radar data to include information about the dipole moment of the antenna; a new elastodynamic inversion scheme is even capable of processing the complete pressure and shear wave information as contained in the components of the displacement vector simultaneously, where we compute the necessary synthetic data with the numerical EFIT code (Elastodynamic Finite Integration Technique) as extended to statistically inhomogeneous media in order to validate the inversion algorithm. © 1997 Published by Elsevier Science Ltd.

Keywords: ground probing radar, ultrasonic and electromagnetic imaging, concrete

Nondestructive testing in civil engineering (NDT-CE) comprises the application of electromagnetic wave (microwave) and elastic wave (ultrasound) scattering and inverse scattering[1]. A comparison between several pulse-echo methods for concrete can be found in Reference 2. This paper concentrates on three items:

1. Application of the electromagnetic vector imaging algorithm HD-POFFIS to locate metal ducts in reinforced concrete (HD-POFFIS: Hertzian Dipole Physical Optics Far-Field Inverse Scattering),
2. Numerical modelling of elastic wave propagation and scattering in concrete with the EFIT code (EFIT: Elastodynamic Finite Integration Technique) to get a better understanding of the wave phenomena in concrete,
3. Application of the elastodynamic vector imaging scheme EL-FT-SAFT (EL-FT-SAFT: Elastodynamic Fourier Transform Synthetic Aperture Focusing Technique) in order to get information about the geometrical dimensions of a concrete structure like the thickness, or to detect voids or delaminations in a metal duct.

Figure 1 shows a typical reinforced concrete sample with a metal duct (diameter $D = 10\,\text{cm}$) and a mesh reinforcement (mesh size 18 cm) covering only one half of the sample. The metal duct is filled with mortar. Relevant parameters of the concrete are: strength category B45; Portland blastfurnace cement HOZ35L; grading curve AB8; total water/cement ratio 0.48. At first we apply the electromagnetic vector imaging algorithm HD-POFFIS to measurements, which were made with a commercial ground-probing pulsed radar by Dr Maierhofer and the Bundesanstalt für Materialforschung und -prüfung (BAM) in Berlin. Then we model the elastic wave propagation and scattering in concrete with the numerical modelling code EFIT in order to understand the physical wave effects in more detail. Finally we apply the elastodynamic image scheme EL-FT-SAFT to a modelled rf-data field in order to determine the thickness of a concrete sample which is under investigation.

Electromagnetic waves applied to concrete: NDT-CE with microwaves

Electromagnetic waves in the time domain (variable t) are governed by Maxwell's equations[3]. These read in integral form for a finite surface S with the contour C:

$$\iint_S \frac{\partial}{\partial t}\underline{\mathbf{B}}(\underline{\mathbf{R}}, t)\cdot\underline{\mathbf{n}}\mathrm{d}S = -\oint_C \underline{\mathbf{E}}(\underline{\mathbf{R}}, t)\cdot\underline{\mathbf{s}}\mathrm{d}R \qquad (1)$$

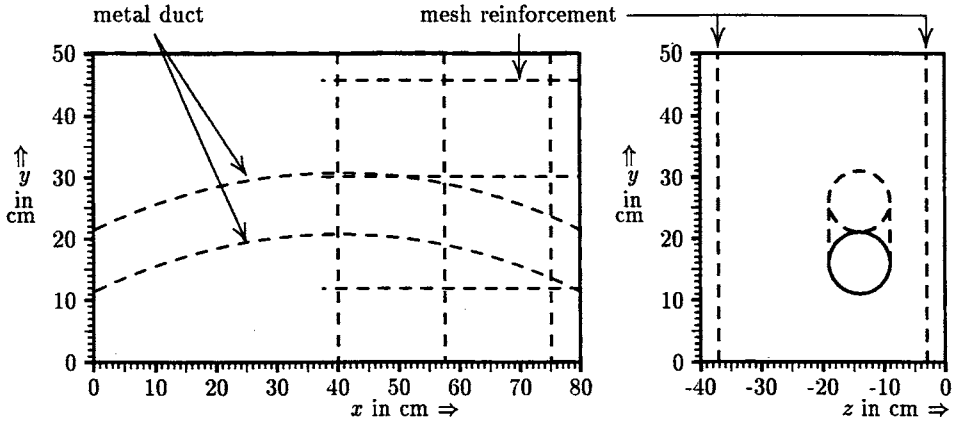

Figure 1 Reinforced concrete sample with a size of 80 cm × 50 cm × 40 cm ($\epsilon_r \simeq 7$) with an embedded metal duct (9 cm deep) and mesh reinforcement (3 cm and 37 cm deep)

$$\iint_S \frac{\partial}{\partial t}\underline{\mathbf{D}}(\underline{\mathbf{R}},t)\cdot\underline{\mathbf{n}}\mathrm{d}S = \oint_C \underline{\mathbf{H}}(\underline{\mathbf{R}},t)\cdot\underline{\mathbf{s}}\mathrm{d}R - \iint_S \underline{\mathbf{J}}(\underline{\mathbf{R}},t)\cdot\underline{\mathbf{n}}\mathrm{d}S \qquad (2)$$

where $\underline{\mathbf{R}}$ is the vector of position, $\underline{\mathbf{B}}$ is the magnetic flux density vector, $\boldsymbol{E}$ is the electric field strength, $\boldsymbol{D}$ is the electric flux density vector, $\boldsymbol{H}$ is the magnetic field strength, $\boldsymbol{J}$ is the electric current density vector, $\boldsymbol{n}$ is the outward normal unit vector of S and $\boldsymbol{s}$ is the tangential vector of C. We model concrete as a non-magnetic non-dissipative isotropic material which is homogeneous with respect to the relative permittivity ϵ_r. Then the electromagnetic constitutive equations are given by:

$$\underline{\mathbf{B}}(\underline{\mathbf{R}},t) = \mu_0\underline{\mathbf{H}}(\underline{\mathbf{R}},t), \qquad \underline{\mathbf{D}}(\underline{\mathbf{R}},t) = \epsilon_r\epsilon_0\underline{\mathbf{E}}(\underline{\mathbf{R}},t) \qquad (3)$$

where μ_0 is the permeability and ϵ_0 is the permittivity of free space; hence, we neglect the finite permeability of Portland cement due to iron content.

The above integral version of Maxwell's equations is the basis for the finite integration technique (FIT) which results in the MAFIA code as a general electromagnetic modelling program[18]. Even if this version is in every textbook on electromagnetic waves, we rewrite the equations here because our numerical EFIT code is close to FIT, and hence it is based on an integral version of the equations of elastic wave motion, which is not so popular.

Inverse scattering

We assume that the metal duct and the rebars of the mesh reinforcement are conductors with infinite conductivity $\sigma = \infty$. In order to locate the metal duct in reinforced concrete we apply a commercial ground-probing pulsed radar, which has been modified in some details. The antenna is a microstrip butterfly antenna with a centre frequency of $f_c = 900\,\mathrm{MHz}$ and a bandwidth of $B = 1\,\mathrm{GHz}$. The size of the antenna is 18 cm × 32 cm. An outline of the antenna geometry is given in Figure 2. The butterfly antenna is approximated by an electric dipole $\underline{\mathbf{p}} = p_0(\omega)\hat{\underline{\mathbf{p}}}$ with the unit vector $\hat{\underline{\mathbf{p}}}$ and the spectrum $p_0(\omega)$. The time history of the excitation pulse is given by the first derivative of a Gaussian function. Based on linear physical optics (PO) within the Kirchhoff approximation we have derived the following vector backprojection algorithm in the time domain for the illuminated top surface of the singular function:

$$\gamma_u^{EM}(\underline{\mathbf{R}}) = \frac{8\sqrt{\epsilon_r}}{Z_0 c_0}\iint_{S_M}\frac{(\underline{\mathbf{R}}'-\underline{\mathbf{R}})\cdot\underline{\mathbf{n}}'}{|\underline{\mathbf{R}}-\underline{\mathbf{R}}'|^2-[\hat{\underline{\mathbf{p}}}\cdot(\underline{\mathbf{R}}-\underline{\mathbf{R}}')]^2} \times \hat{\underline{\mathbf{p}}}\cdot\underline{\mathbf{E}}^{sca}\left(\underline{\mathbf{R}}',\tilde{\underline{\mathbf{t}}}=\frac{2\sqrt{\epsilon_r}}{c_0}|\underline{\mathbf{R}}-\underline{\mathbf{R}}'|\right)\mathrm{d}S' \qquad (4)$$

A singular function of a surface has a delta-function property on that surface: it peaks there in a way that a three-dimensional volume integral over all space reduces to a surface integral due to a generalized sifting property. This means that we have solved the inverse scattering problem once we have determined the singular function of the scatterer under concern.

This inversion scheme is called Hertzian Dipole Physical Optics Far-field Inverse Scattering (HD-POFFIS)[1,4]. A scalar version of POFFIS can be found in Reference 5 and for further reading about inverse scattering see references 6, 7. We applied the formula (4) to measurements of the concrete sample shown in Figure 1. The phase velocity in concrete is $c_{ph}^{con} = c_0/\sqrt{7} = 1.134 \times 10^8\,\mathrm{m/s}$ with a relative permittivity $\epsilon_r \simeq 7$ resulting in a wavelength of $\lambda_c^{con} = 12.6\,\mathrm{cm}$ at centre frequency. We measured 21 points in the x-direction and 498 points in the y-direction, and at each point 512 time samples were recorded. Then we applied a linear interpolation in the x-direction and we took every sixth sample in the y-direction yielding a 3D data field of 121 × 84 × 512 samples. Figure 2 shows three orthogonal slices and Figure 3 shows an isosurface of the reconstructed illuminated top surface of the singular function. Both figures exhibit a good agreement with the given geometry of the metal duct (see Figure 1). Because of shielding effects of the mesh reinforcement on the right half of the sample, the right part of the metal duct is

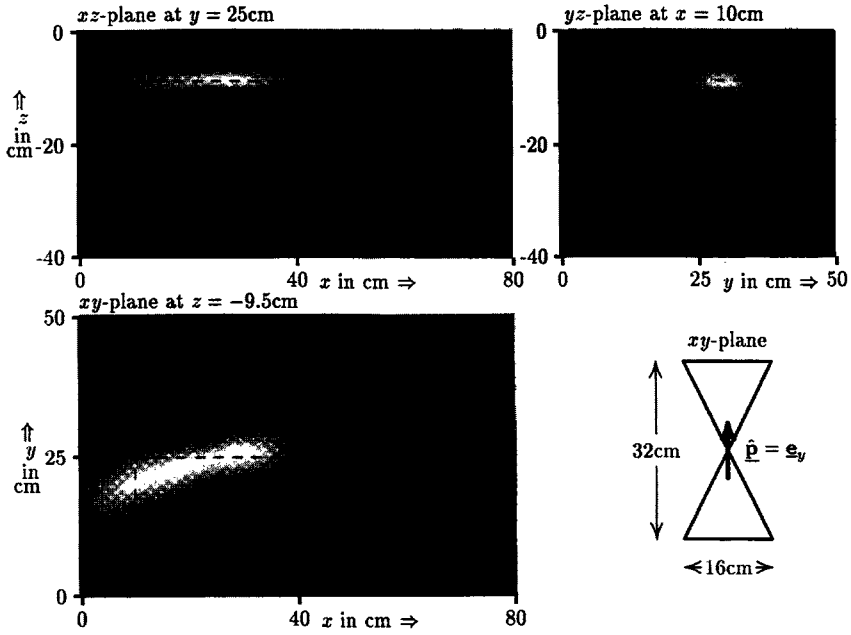

Figure 2 Three orthogonal slices of the reconstructed illuminated top surface of the singular fuction $\gamma_u^{EM}(\underline{\mathbf{R}})$, showing the metal duct in the reinforced concrete. Lower right: geometry of the microstrip butterfly antenna

missing in the reconstruction. To test the influence of the vector character of this inversion scheme we made a further reconstruction with a purposely wrong dipole direction $\hat{\underline{\mathbf{p}}} = \underline{\mathbf{e}}_x$. This leads to some defocusing effects which are also present if we restrict ourselves to the scalar FT-SAFT imaging algorithm[8,9], which does not at all account for the vector character of the electromagnetic field.

Elastic waves applied to concrete: NDT-CE with ultrasound

Elastic waves in concrete are governed by Cauchy's equation of motion and the equation of deformation rate[10,11]. For the sake of the applicability of the finite integration technique, these equations are given in the somewhat unusual integral form for a finite volume V with the surface S by:

$$\iiint_V \frac{\partial}{\partial t}\underline{\mathbf{p}}(\underline{\mathbf{R}},t)\mathrm{d}V = \oiint_S \underline{\mathbf{n}}\cdot\underline{\underline{\mathbf{T}}}(\underline{\mathbf{R}},t)\mathrm{d}S + \iiint_V \underline{\mathbf{f}}(\underline{\mathbf{R}},t)\mathrm{d}V \tag{5}$$

$$\iiint_V \frac{\partial}{\partial t}\underline{\underline{\mathbf{S}}}(\underline{\mathbf{R}},t)\mathrm{d}V = \oiint_S \mathrm{sym}\{\underline{\mathbf{nv}}(\underline{\mathbf{R}},t)\}\mathrm{d}S + \iiint_V \underline{\underline{\mathbf{h}}}(\underline{\mathbf{R}},t)\mathrm{d}V \tag{6}$$

where $\underline{\mathbf{p}}$ is the momentum density vector, $\underline{\underline{\mathbf{T}}}$ is the second rank stress tensor, $\underline{\underline{\mathbf{S}}}$ is the second rank strain tensor, $\underline{\mathbf{v}}$ is the particle velocity vector, $\underline{\mathbf{f}}$ is the source of force density, $\underline{\underline{\mathbf{h}}}$ is the source of the second rank deformation rate tensor, $\underline{\mathbf{n}}$ is the outward normal unit vector of S and sym $\{\underline{\mathbf{nv}}\}$ denotes the symmetric part of the dyad $\underline{\mathbf{nv}}$. We assume concrete to be a non-dissipative isotropic

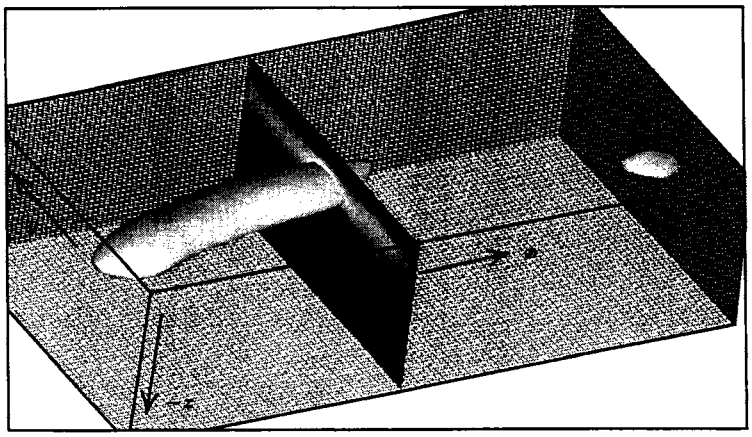

Figure 3 Isosurface of the reconstructed illuminated top surface of the singlar function $\gamma_u^{EM}(\underline{\mathbf{R}})$, showing the metal duct in the reinforced concrete

inhomogeneous material. Accordingly the material properties are given by the following constitutive equations

$$\underline{\mathbf{p}}(\underline{\mathbf{R}},t)=\rho_0(\underline{\mathbf{R}})\underline{\mathbf{v}}(\underline{\mathbf{R}},t),\qquad \underline{\underline{\mathbf{S}}}(\underline{\mathbf{R}},t)=\underline{\underline{\underline{\underline{\mathbf{s}}}}}(\underline{\mathbf{R}}):\underline{\underline{\mathbf{T}}}(\underline{\mathbf{R}},t) \tag{7}$$

where ρ_0 is the volume density of mass at rest and $\underline{\underline{\underline{\underline{\mathbf{s}}}}}$ is the compliance tensor of rank four. For the isotropic case the compliance tensor reads:

$$\underline{\underline{\underline{\underline{\mathbf{s}}}}}^{\mathrm{iso}}(\underline{\mathbf{R}})=\Lambda(\underline{\mathbf{R}})\underline{\underline{\mathbf{II}}}+M(\underline{\mathbf{R}})(\underline{\underline{\mathbf{II}}}^{1324}+\underline{\underline{\mathbf{II}}}^{1342}) \tag{8}$$

with

$$\Lambda(\underline{\mathbf{R}})=\frac{\lambda(\underline{\mathbf{R}})}{2\mu(\underline{\mathbf{R}})[3\lambda(\underline{\mathbf{R}})+2\mu(\underline{\mathbf{R}})]},\qquad M(\underline{\mathbf{R}})=\frac{1}{4\mu(\underline{\mathbf{R}})} \tag{9}$$

where λ, μ are Lamé's constants and $\underline{\underline{\mathbf{I}}}$ is the unit dyadic or the idemfactor.

EFIT modelling

For the numerical modelling of elastic waves in concrete we use the elastodynamic finite integration technique (EFIT). A description of this method is given in References 12, 13 and first examples of the numerical modeling of elastic waves (ultrasound) in concrete and applications of an inverse scattering algorithm can be found in References 14, 15.

Due to the additives and air inclusions which may occur in the material, concrete is very inhomogeneous. Usually concrete consists of cement and several additives like basalt, plaster, biatitgranite. The maximum aggregate size, grading curve, water/air concentration of every additive can vary. Figure 4 illustrates on the left-hand side the utilized concrete model for the EFIT modelling and on the right-hand side an enlarged detail drawing. The base material is hydrated cement and the additives are biatitgranite, basalt and plaster with a maximum aggregate size of 8 mm and we used the grading curve B8. The additives are modeled by 60 000 ellipses varying statistically in size, orientation and additives; details can be found in reference 16. Every material cell of the EFIT grid can cover different material parameters. The total number of the ellipses is only limited by the number of material cells. In this example we have $2000 \times 2000 = 4 \times 10^6$ material cells. The concentration of each aggregate size refers to the grading curve B8. We used a normal pressure probe with a centre frequency of $f_c = 80\,\mathrm{kHz}$. The time history of the pulse is modelled by a raised cosine with two cycles. The probe has a diameter of $D = 5\,\mathrm{cm}$. Snapshots of the elastic wavefield are shown in Figure 5. We recognize at t_1 the near-field of the excited elastic wavefield. At t_2 we identify a prominent pressure wave followed by a shear wave, head waves, and Rayleigh waves at the top surface, the latter having a stress-free boundary condition. Because of the open boundary condition of the Higdon type of the left and right boundaries, a concrete plate of infinite extent in the horizontal direction is actually modelled. At the bottom boundary we applied a stress-free boundary condition also. The backwall echo of the pressure wave shows up very clearly at t_3, which propagates back to the top surface where it is recorded by the normal pressure probe.

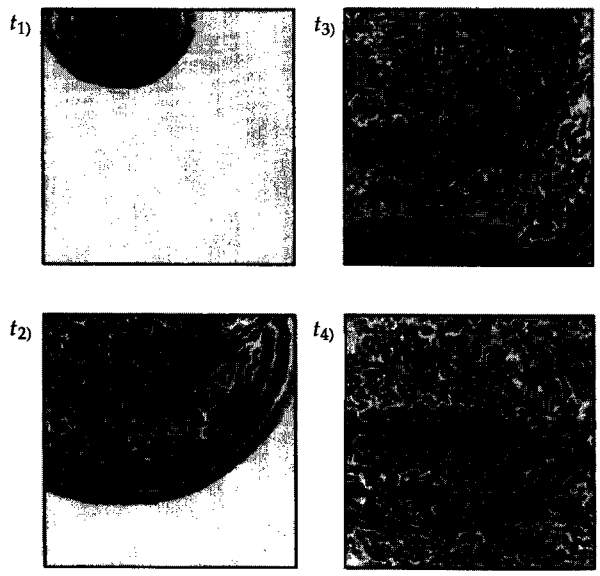

Figure 5 EFIT-$|v|$-snapshots of the elastic wavefield in concrete

Inverse scattering

To tackle the inverse scattering problem in elastodynamics we use an elastic vector imaging algorithm which

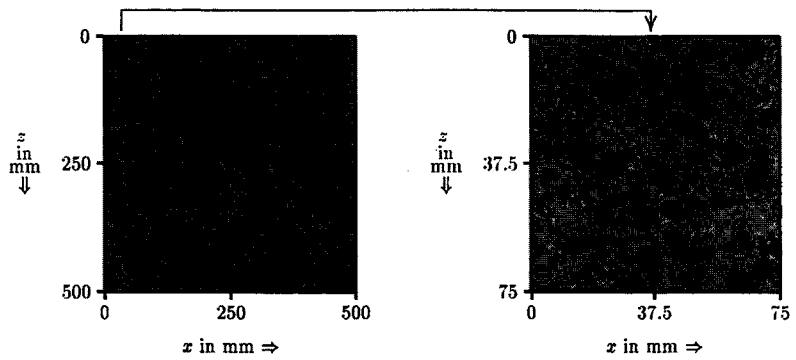

Figure 4 Left: concrete model for EFIT modelling; right: detail drawing

we called the ELastic Fourier Transform Synthetic Aperture Focusing Technique (EL-FT-SAFT). It is based on the linear elastic far-field inversion including a near-field far-field transformation .The formulation of the diffraction imaging algorithm is based on Huygens' principle. This reads in linear elastodynamics for a volume V with the closed surface S:

$$\oiint_S \underline{\mathbf{n}}' \cdot [\underline{\underline{\mathbf{T}}}(\underline{\mathbf{R}}', \omega) \cdot \underline{\underline{\mathbf{G}}}(\underline{\mathbf{R}} - \underline{\mathbf{R}}', \omega) - \underline{\mathbf{u}}(\underline{\mathbf{R}}', \omega) \cdot \underline{\underline{\underline{\mathbf{\Sigma}}}}'(\underline{\mathbf{R}} - \underline{\mathbf{R}}', \omega)] \mathrm{d}S' + \iiint_V \underline{\mathbf{f}}(\underline{\mathbf{R}}', \omega) \cdot \underline{\underline{\mathbf{G}}}(\underline{\mathbf{R}} - \underline{\mathbf{R}}', \omega) \mathrm{d}V' = \begin{cases} \underline{\mathbf{u}}(\underline{\mathbf{R}}, \omega) & \underline{\mathbf{R}} \in V \backslash S \\ \frac{1}{2}\underline{\mathbf{u}}(\underline{\mathbf{R}}, \omega) & \underline{\mathbf{R}} \in S \\ \underline{\mathbf{0}} & \underline{\mathbf{R}} \in \mathbb{R}^3 \backslash V \end{cases} \tag{10}$$

with $\underline{\mathbf{n}}'$ being the outward normal unit vector of the surface S, $\underline{\underline{\underline{\mathbf{\Sigma}}}}$ is the triadic and $\underline{\underline{\mathbf{G}}}$ the dyadic displacement Green function of free space[12]. Application of the equivalence principle leads to a representation of the scattered field on the surface S. The particle velocity vector of the scattered field is then given by:

$$\underline{\mathbf{u}}^{\mathrm{sca}}(\underline{\mathbf{R}}, \omega) = \oiint_S \{\underline{\mathbf{u}}(\underline{\mathbf{R}}', \omega) \cdot [\underline{\mathbf{n}}' \cdot \underline{\underline{\underline{\mathbf{\Sigma}}}}'(\underline{\mathbf{R}}' - \underline{\mathbf{R}}', \omega)] - \underline{\mathbf{n}}' \cdot \underline{\underline{\mathbf{T}}}(\underline{\mathbf{R}}', \omega) \cdot \underline{\underline{\mathbf{G}}}(\underline{\mathbf{R}} - \underline{\mathbf{R}}', \omega)\} \mathrm{d}S' \tag{11}$$

Introducing the far-field approximation in Equation (11) we get the definition of the linearized far-field scattering amplitude for perfectly stress-free scattering surfaces $\underline{\mathbf{C}}_{s\alpha\beta}(\hat{\underline{\mathbf{R}}}, \omega)$. Then, with the approximation of physical elastodynamics (PE) as compared to physical optics, the illuminated part of the singlular function in the bistatic or pitch-catch mode of operation is given by the elastodynamic far-field algorithm in K-space[17], the spatial three-dimensional Fourier space of the scatterer:

$$\tilde{\gamma}_{\mathrm{u}}^{\mathrm{E}}(\underline{\mathbf{K}}) = \frac{1}{|\underline{\mathbf{V}}_{\alpha\beta}^{\mathrm{PE,bi}}(\hat{\underline{\mathbf{R}}}, \hat{\underline{\mathbf{k}}}_{\mathrm{i}}, \omega)|^2} \underline{\mathbf{V}}_{\alpha\beta}^{\mathrm{PE,bi}}(\hat{\underline{\mathbf{R}}}, \underline{\mathbf{k}}_{\mathrm{i}}, \omega) \cdot \underline{\mathbf{C}}_{s\alpha\beta}(\hat{\underline{\mathbf{R}}}, \omega), \quad \alpha, \beta = P, S \tag{12}$$

with

$$\underline{\mathbf{V}}_{\alpha\beta}^{\mathrm{PE,bi}}(\hat{\underline{\mathbf{R}}}, \hat{\underline{\mathbf{k}}}_{\mathrm{i}}, \omega) = \frac{1}{2\pi} R_{\mathrm{f}} \underline{\mathbf{u}}_{0\alpha}(\hat{\underline{\mathbf{k}}}_i, \omega) \underline{\mathbf{n}}_{\alpha\beta}(\hat{\underline{\mathbf{R}}}, \hat{\underline{\mathbf{k}}}_{\mathrm{i}}) : \underline{\underline{\underline{\mathbf{T}}}}_{\beta}^{\mathrm{far}}(\hat{\underline{\mathbf{R}}}, \omega) \tag{13}$$

where α and β denote the exciting and receiving mode, R_{f} is the reflection coefficient, $\underline{\mathbf{u}}_{0\alpha}$ is the vector frequency spectrum of the transmitted signal, $\underline{\mathbf{n}}_{\alpha\beta}$ is the stationary phase normal and:

$$\underline{\underline{\underline{\mathbf{T}}}}_{\mathrm{P}}^{\mathrm{far}}(\hat{\underline{\mathbf{R}}}, \omega) = -\frac{jk_{\mathrm{P}}^3}{\rho_0 \omega^2} (\lambda \underline{\underline{\mathbf{I}}} \hat{\underline{\mathbf{R}}} + 2\mu \hat{\underline{\mathbf{R}}} \hat{\underline{\mathbf{R}}} \hat{\underline{\mathbf{R}}}) \tag{14}$$

$$\underline{\underline{\underline{\mathbf{T}}}}_{\mathrm{S}}^{\mathrm{far}}(\hat{\underline{\mathbf{R}}}, \omega) = -\frac{jk_{\mathrm{S}}^3}{\rho_0 \omega^2} \mu (\hat{\underline{\mathbf{R}}} \underline{\underline{\mathbf{I}}} + \hat{\underline{\mathbf{R}}} \underline{\underline{\mathbf{I}}}^{213} - 2\hat{\underline{\mathbf{R}}} \hat{\underline{\mathbf{R}}} \hat{\underline{\mathbf{R}}}) \tag{15}$$

are the prefactors of the triadic far-field Green function:

$$\underline{\underline{\underline{\mathbf{\Sigma}}}}_{\beta}^{\mathrm{far}}(\hat{\underline{\mathbf{R}}}, \omega) = \underline{\underline{\underline{\mathbf{T}}}}_{\beta}^{\mathrm{far}}(\hat{\underline{\mathbf{R}}}, \omega) G_{\beta}^{\mathrm{far}}(\hat{\underline{\mathbf{R}}}, \omega), \qquad \beta = P, S \tag{16}$$

$G_{\beta}^{\mathrm{far}}(\hat{\underline{\mathbf{R}}}, \omega)$ denoting the scalar Green function. $\gamma_{\mathrm{u}}^{\mathrm{E}}(\underline{\mathbf{R}})$ is then calculated by applying a three-dimensional inverse Fourier transform with respect to $\underline{\mathbf{K}}$. Equation (12) represents the essence of the elastic vector imaging algorithm EL-FT-SAFT. Figure 6 shows on the left side the rf-data field which has been 'recorded' (modelled) at the top surface of the concrete sample and on the right side the EL-FT-SAFT reconstruction for an assumed average sound velocity c_{M}, which is required by the inversion scheme. The backwall of the concrete sample can be clearly identified. The thickness of the sample appears to be smaller because the averaged sound velocity c_{M} does not properly account for all the multiple scattering by the concrete inhomogeneities, which determine the real physical wave speed.

References

1 **Marklein, R., Langenberg, K. J., Bärmann R. and Brandfaß, M.,** Ultrasonic and electromagnetic wave propagation and inverse scattering applied to concrete. In *Review of Progress in Quantitative Nondestructive Evaluation*, eds. D. O. Thompson and D. E. Chimenti **15**, Plenum Press, New York, 1996, pp. 1839–1846.

2 **Krause, M., Bärmann, R., Frielinghaus, R., Kretzschmar, F., Kroggel, O., Langenberg, K. J., Maierhofer, C., Müller, W., Neisecke, J., Schickert, M., Schmitz, V., Wiggenhauser, H. and Wollbold, F.,** Comparison of pulse-echo-methods for concrete. In *Proc. Int. Symp. on Non-Destructive Testing in Civil Engineering*, eds. G. Schickert and H. Wiggenhauser, Deutsche Gesellschaft für Zerstörungsfreie Prüfung, Berlin (1995) pp. 281–295.

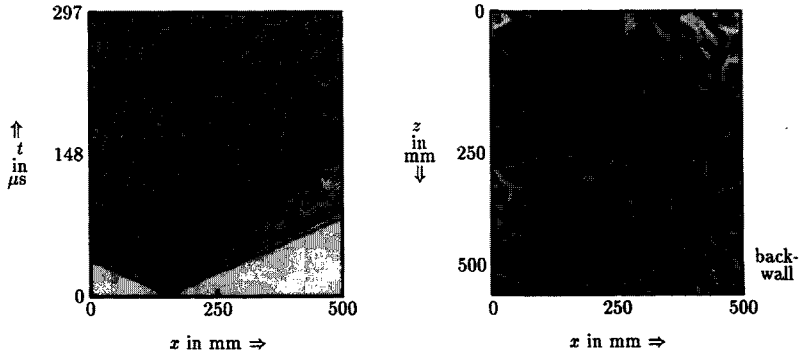

Figure 6 Modelled rf-data field (left) and EL-FT-SAFT reconstruction (right)

3 **Chen, H. C.,** *Theory of Electromagnetic Waves: A Coordinate-Free Approach*, McGraw-Hill, New York, 1983.

4 **Brandfaß, M.,** Inverse Beugungstheorie elektromagnetischer Wellen: Algorithmen und numerische Realisierung, Ph. D. Thesis, University of Kassel, Kassel , 1996.

5 **Bojarski, N. N.,** A survey of physical optics inverse scattering. *IEEE Trans. Ant. Propagat.* 1982, **AP-30**, 980–989.

6 **Langenberg, K. J.,** Introduction to the special issue on inverse problems. *Wave Motion*, 1989, **11**, 99–112.

7 **Langenberg, K. J., Brandfaß, M., Fellinger, P. Gurke, T. and Kreutter, T.,** A unified theory of multidimensional electromagnetic vector inverse scattering within the Kirchhoff or Born approximation. In *Radar Target Imaging*, eds. W. M. Boerner and H. Überall, Springer-Verlag, Berlin, 1994 pp. 113–151.

8 **Mayer, K., Marklein, R., Langenberg, K. J. and Kreutter, T.,** Three-dimensional imaging system based on Fourier transform synthetic aperture focusing technique. *Ultrasonics*, 1990, **28**, 241–255.

9 **Langenberg, K. J., Fellinger, P., Marklein, R., Zanger, P., Mayer, K. and Kreutter, T.,** Inverse methods and imaging. In *Evaluation of Materials and Structures by Quantitative Ultrasonics*, ed. J. D. Achenbach, Springer-Verlag, Vienna, 1993, pp. 317–398.

10 **Auld, B. A.,** *Acoustic Fields and Waves in Solids*, Krieger, Malabar, 1990.

11 **van der Hijden, J. H. M. T.,** *Propagation of Transient Elastic Waves in Stratified Anisotropic Media*, North-Holland, Amsterdam, 1987.

12 **Fellinger, P.,** Ein Verfahren zur numerischen Behandlung elastischer Wellenausbreitungsprobleme im Zeitbreich durch direkte Diskretisierung der elastodynamischen Grundgleichungen, Ph. D. Thesis, University of Kassel, Kassel, 1989.

13 **Fellinger, P., Marklein, R., Langenberg, K. J. and Klaholz, S.,** Numerical modeling of elastic wave propagation and scattering with EFIT–Elastodynamic Finite Integration Technique. *Wave Motion*, 1995, **21**, 47–66.

14 **Marklein, R., Bärmann, R. and Langenberg, K. J.,** Die AFIT- und EFIT-Codes zur Modellierung von Ultraschallwellen in dissipativen oder dämpfenden Materialien. In *Proc. DGZfP-Jahrestagung 1994*, DGZfP, Berlin, 1995, pp. 409–421.

15 **Marklein, R., Bärmann, R. and Langenberg, K. J.,** The ultrasonic modeling code EFIT as applied to inhomogeneous dissipative isotropic and anisotropic media. In *Review of Progress in Quantitiative Nondestructive Evaulation 1994*, vol 14, eds. D. O. Thompson and D. E. Chimenti, Plenum Press, New York, 1995, pp. 251–258.

16 **Irmer, S. and Müller, H.,** Ultraschallmodellierung mit dem EFIT-Code zur zerstörungsfreien Prüfung an Beton, Projektarbeit, University of Kassel, Kassel, 1995.

17 **Bärmann, R. and Langenberg, K. J.,** Elastodynamic far-field inversion for perfect scatterers, Internal Report of the Dept. of Electrical Eng. of the University of Kassel, Germany, 1995.

18 **Bartsch, M., Dehler, M., Dohlus, M., Ebeling, F., Hahne, P., Klatt, R., Krawczyk, F., Marx, M., Min, Zhang, Pröpper, T., Schmitt, D., Schütt, P., Steffen, B., Wagner, B., Weiland, T. Wipf, S. G., and Wolter, H.** Solution of Maxwells' equations. *Computer Physics Communications*, 1992, **72**, 22.